Check for updates

Journal of
Intelligent Material
Systems and Structures

Review Article

Journal of Intelligent Material Systems and Structures
2018, Vol. 29(11) 2309–2323
© The Author(s) 2018
Reprints and permissions:
sagepub.co.uk/journalsPermissions.nav
DOI: 10.1177/1045389X18758179
journals.sagepub.com/home/jim
SAGE

Vibration control of a flexible rotor suspended by shape memory alloy wires

Marco Túlio Santana Alves[1], Valder Steffen Jr[2], Marina Castro dos Santos[3], Marcelo Amorim Savi[3], Søren Enemark[4] and Ilmar Ferreira Santos[4]

Abstract

The present contribution is devoted to the study of the influence of shape memory alloys on the dynamic behavior of flexible rotors. In this sense, a suspension composed by pseudoelastic shape memory alloy wires that are connected to a rotor-bearing test rig was designed. To evaluate the performance of the system, both numerical and experimental investigations are carried out. The suspension stiffness can vary, especially in the pseudoelastic region, so that this variation takes place per a hysteretic cycle denoting energy dissipation whenever the loading magnitude is sufficient to induce a phase transformation. The constitutive model used to describe the shape memory alloy behavior is a modified version of the Brinson model for the one-dimensional case. To provide all thermomechanical properties of shape memory alloy wire, a complete characterization process was performed. Due to numerical reasons, the size of the model of the rotating system was reduced. Finally, numerical and experimental results demonstrate the success of shape memory alloy applied to the suspension of rotating machines as an interesting alternative for vibration control.

Keywords

Rotordynamics, shape memory alloys, passive and semi-active control, smart rotors, vibration control

Introduction

The use of smart materials with the intention of mitigating vibration in rotating machines has been increasingly investigated by various researchers. However, there is a category of material still not fully explored for this purpose, namely, the shape memory alloy (SMA), which points out a new direction in the field of vibration control of rotating machines. SMA exhibits characteristics of shape memory and pseudoelasticity depending on the thermomechanical state. Thus, its stiffness can vary, especially in the pseudoelastic region, where this variation takes place, per a hysteretic cycle denoting energy dissipation, once the crystallographic structure migrates from austenite to martensite (and vice versa) whenever the loading magnitude is sufficient to induce this phase transformation.

These capabilities of SMA with respect to rotating machines have been previously investigated in a few publications. Nagaya et al. (1987) are some of the pioneers in using this family of materials applied to vibration control of rotors. They used SMA springs to change the bearing support stiffness by either heating or cooling the springs. Liu et al. (1994) investigated and proposed the use of SMA wires attached to the housing of hydrodynamic bearing to control the vibration, so that its stiffness reduces (softening) while the rotor accelerates and increases (hardening) while the rotor slows down. Both the behaviors are nonlinear, and the pseudoelastic SMA wires play the role of energy dissipation device. Nie and Yan (2000) designed a smart support system to pass through critical speeds of an aeroengine. The principle of operation is based on an active switching of stiffnesses, where the SMA wires work as actuators. In this way, the engine has two different stiffness connections, so that this characteristic is

[1]Federal University of Bahia, Salvador, Brazil
[2]School of Mechanical Engineering, Federal University of Uberlândia, Uberlândia, Brazil
[3]Federal University of Rio de Janeiro, Rio de Janeiro, Brazil
[4]Technical University of Denmark, Kongens Lyngby, Denmark

Corresponding author:
Valder Steffen Jr, School of Mechanical Engineering, Federal University of Uberlândia, Av. João Naves de Ávila, 2121, Uberlândia—MG 38408-902, Brazil.
Email: vsteffen@ufu.br

useful to switch conveniently the stiffness in *run-up* and *run-down* operations to reduce the vibration amplitude when crossing the critical speeds. In their work, Gupta et al. (2003) propose the employment of SMA wires embedded in shafts composed by epoxy resin and fiberglass to modify their stiffness. The wires are stretched before they are embedded into the shaft so that an axial compression is induced, increasing its stiffness. Then, using electric current, it is possible to change the shaft stiffness conveniently. He et al. (2007a, 2007b) proposed a self-optimizing support system where SMA springs are used to construct a bearing pedestal. In addition, using the principle of dynamic vibration absorbers they calculated and changed the stiffness of the pedestal to set the rotor-bearing system close to the anti-resonance condition. Lees et al. (2007) applied SMA to a bearing pedestal by means of a winding of wires to change its stiffness by Joule effect. Atepor (2008) applied SMA elements integrated within glass epoxy composite plates and shells resulting the design of a novel smart bearing based on the principle of antagonistic action. Zhu et al. (2009) developed and applied a model based on multi-variate statistical analysis vibration control of rotor systems with SMA. More recently, Borges et al. (2013) used helical springs made of SMA to control the vibration of a flexible rotor. They employed the general concept of dynamic vibration absorbers to model the system, so that the mass of the bearing where the SMA springs are located is considered as the secondary mass. Besides, a control law based on fuzzy logic was employed, in such a way that the transfer function correlates the spring temperature with its stiffness. In the same year, Silva et al. (2013) investigated the behavior of a rotordynamic nonsmooth SMA system where it is modeled as a Jeffcott rotor with two degrees of freedom (DOFs). The focus relied on a comparison between the rotor responses with linear elastic support and those from the rotor with an SMA support. In addition, the dependence on the temperature was also investigated. It is noteworthy to mention that both compression and tension actions on the SMA element were allowed. Ma et al. (2014) described the design, manufacturing, and evaluation of a smart support with elements of SMA. Based on this concept, the support can provide both variable stiffness and damping with respect to three parameters, namely: temperature, vibration amplitude, and excitation frequency. Enemark et al. (2015) investigated experimentally how pseudoelastic SMA springs influence the dynamic behavior of a rotor-bearing system with low damping due to passive magnetic bearings. It was observed that the higher the temperature, the stiffer the support. In addition, the hysteretic behavior of the system was evaluated. Therefore, both the amplitude responses through the critical speeds and the mode shapes were changed in order to reduce vibration. As an extended version of above-mentioned paper, Enemark and Santos (2016b) presented a deeper analysis by comparing theoretical and experimental results proving, in terms of vibration suppression, the advantage of applying SMA to a rotor-bearing system. Yogaraju et al. (2016), based on experimental studies, observed that SMA can be used as a medium to apply necessary forces at identified locations to obtain the desired profile shapes for a multi-lobe bearing configuration facilitating the development of semi-active journal bearings. Finally, Yuan et al. (2017) presented a very detailed review about actuators driven by SMA, more specifically rotary actuator, highlighting its specificities and potentialities for new applications in the future. Thus, a rotating machine could be benefited by some of the concepts explored.

The present contribution deals with study of dynamic behavior of a horizontal rotor-bearing system suspended by SMAs pseudoelastic wires, in order to verify the feasibility of either passive or semi-active control devices for rotating machines in the future. In terms of control, the strategy is based upon the change of stiffness by heating/cooling the suspension and the addition of some damping by cyclic phase transformation due to mechanical loading. The performance of the proposed system is investigated for the following conditions: rotor at steady-state motion with several temperatures, rotor at steady-state motion with varying temperature and transient motion with several temperatures. To be effective, the suspension by pre-tensioned wire (SPW) is mounted along the horizontal plane, and it is located at the position of one of the rotor bearings. To reduce the computational cost, the size of the rotor model obtained from finite element method (FEM) is reduced by neglecting the higher modes. The constitutive model used to describe the SMA behavior is a modified version of the model by Brinson for the one-dimensional (1D) case, as performed by Enemark et al. (2014).

This article is organized according to five sections, as follows. After a brief overview presented in the introduction, the rotor model is derived using the FEM; the concept of suspension system, its characteristics, and its modeling are then presented; a comparison between numerical and experimental results is discussed; and finally, the conclusions are summarized.

The experimental apparatus

Figure 1 depicts an overview of the experimental apparatus, highlighting the main parts of the test rig. Basically, it is encompassed by a flexible rotor-bearing system, a heating device, and the rotor suspension. As designed by Alves (2015), the suspension, composed of pre-tensioned wires, is encapsulated inside a heating chamber to keep the temperature of the air from the heat gun under control, as detailed in Figure 2. The main physical properties related to the rotor-bearing

Table 1. Physical characteristics of rotor-bearing system and imbalance.

Shaft	
Material	Steel
Diameter (mm)	6
Length (mm)	581
Young's modulus (GPa)	205
Density (kg/m^3)	7800
Mass (kg)	0.129
Disk	
Material	Steel
Diameter (mm)	120
Thickness (mm)	11
Mass (kg)	0.860
Bearing #1	
Mass (kg)	0.140
Stiffness (horizontal direction) (N/m)	1.25×10^5
Stiffness (vertical direction) (N/m)	3.83×10^8
Bearing #2	
Mass (kg)	0.407
Stiffness (horizontal direction) (N/m)	1.31×10^4
Stiffness (vertical direction) (N/m)	1.35×10^8
Coupling	
Stiffness (horizontal direction) (N/m)	2.00×10^4
Stiffness (vertical direction) (N/m)	2.60×10^4
Imbalance	
Imbalance (g $\times$ mm)	45.0

system are shown in Table 1. The SMA wires are made of nickel and titanium (Ni-Ti alloy), whose total length is 160 mm. The choice of the wire diameter 0.25 mm was made by considering two reasons, as follows: first, to provide condition to assume isothermal distribution of temperature along the cross-sectional area; second, to make the suspension flexible enough to allow phase transformation through the wire deformation.

The suspension of bearing #2 is composed basically of a bearing housing supported by a flexible frame composed by two steel rulers, as can be seen in Figure 3. In spite of the fact that most of the bearings have similar stiffnesses in both directions, this concept was adopted to allow high amplitude of vibration along to the horizontal plane, since the architecture of the suspension was designed to work on the same plane. Thus, based on strength of materials, a relationship between axial (vertical direction) and flexural (horizontal) stiffnesses (k_z/k_y) can be calculated as follows

$$\frac{k_z}{k_y} = \frac{E_b A_b/L_b}{12E_b I_b/L_b^3} = \frac{E_b wh/L_b}{12E_b(wh^3/12)/L_b^3} = \left(\frac{L_b}{h}\right)^2 \quad (1)$$

where, for the steel ruler, w, h, and L_b are the width, thickness, and length, respectively. In addition, A_b, I_b, and E_b are the cross-sectional area, moment of inertia of area, and Young's modulus, respectively. Therefore, the result shown by equation (1) explains the huge discrepancy in the order of magnitude between the stiffnesses along to horizontal and vertical direction, as presented in Table 1 and depicted schematically in

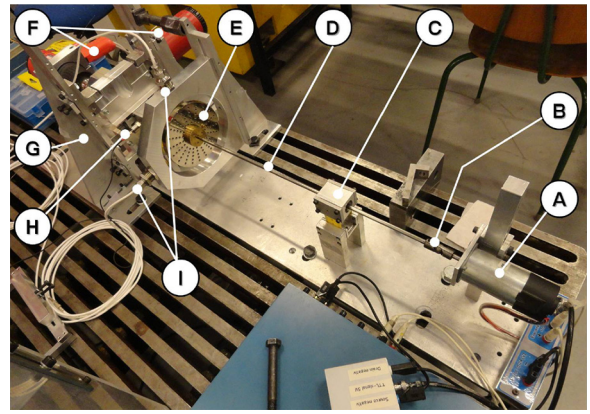

Figure 1. Experimental apparatus: (A) DC motor/encoder; (B) coupling; (C) bearing #1; (D) flexible shaft; (E) disk; (F) heat guns; (G) suspension system; (H) accelerometer; and (I) proximity probes.

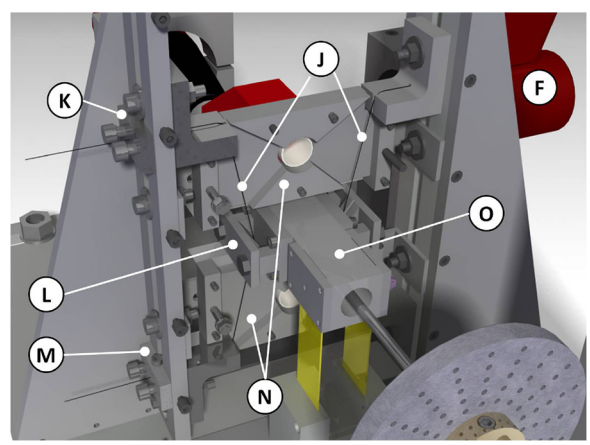

Figure 2. Detailed view of suspension by pre-tensioned wires (SPW): (F) heat gun; (J) PE SMA wires; (K), (L), and (M) tensioners; (N) heating chamber; and (O) bearing #2.

Figure 3. In this article, the ratio $L_b/h = 64$, such that $k_z \simeq 4100\ k_y$. However, it is noteworthy to mention that the stiffnesses presented in Table 1 were obtained after parameter adjustments, as performed by Alves (2015) (see Table 2).

System modeling

The models used to describe the behavior of the complete system are presented separately, according to each sub-system. First, the rotor formulation and its properties are shown. Then, the general characteristics and properties of the suspension, as based on pre-tensioned wires, are discussed. Finally, the truncation criteria and the reduced model of the complete system are presented.

Rotor model

The dynamic response of the considered mechanical system can be modeled using variational mechanics

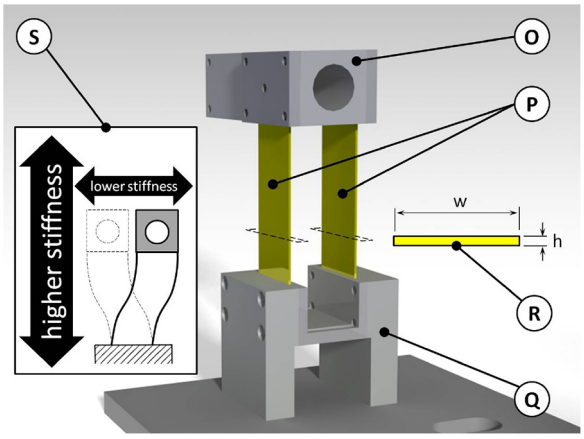

Figure 3. Detailed view of bearing #2: (O) bearing #2's housing; (P) flexible frame; (Q) bearing #2's base; (R) steel ruler's cross section; and (S) schematic comparison between flexural and axial stiffnesses.

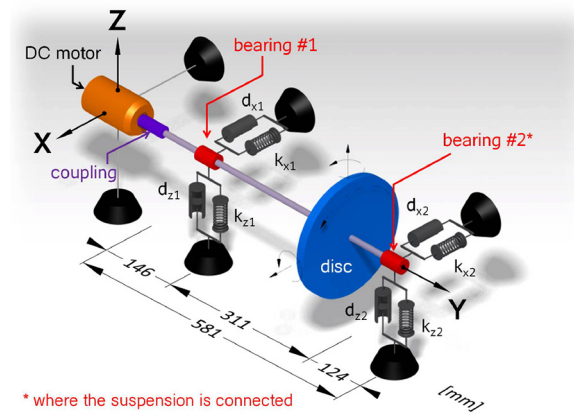

Figure 4. Schematic of the rotor-bearing system.

Table 2. List of equipments and instrumentation installed to the test rig.

Equipment	Brand	Model
DC motor/encoder	RS Components	715-112
Power supply (DC motor)	Bang & Olufsen	SN16A
Acquisition card	D-Space	CP1103
Accelerometer	B&K	Type 4384
Charge amplifier	B&K	Type 2635
Proximity probes	Vibro-Meter	TQ403
Driver (proximity probes)	Vibro-Meter	IQS450
Thermocouple/universal transmitter	PR Electronics	4114
Power supply (universal transmitter)	Mascot	2183—24 VDC/1A
Heat guns	Am-Tech	V2260—230–240 V
Relay transistor	Crydom	CL240D10
Power supply (heat gun motor)	Radiofoni	40VDC/3A

equations as based on the Hamilton's principle. For this aim, the strain energy of the shaft and the kinetic energies of the shaft and disks are calculated. An extension of Hamilton's principle makes possible to include the effect of energy dissipation. The parameters of the bearings are considered in the model using the principle of the virtual work. For computation purposes, the FEM is used to discretize the structure so that the energies calculated are concentrated at the nodal points. Shape functions are used to connect the nodal points. The model obtained as described above is represented mathematically by the set of differential equations (Lalanne and Ferraris, 1997) given by equation (2)

$$\mathbf{M}\ddot{\mathbf{x}} + \left[\mathbf{C} + \dot{\phi}\mathbf{G}\right]\dot{\mathbf{x}} + \left[\mathbf{K} + \ddot{\phi}\mathbf{K}_G\right]\mathbf{x} = \mathbf{F}_u + \mathbf{F}_s \qquad (2)$$

where $\mathbf{x}$ is the vector of generalized displacements; $\mathbf{M}$, $\mathbf{K}$, $\mathbf{K}_G$, $\mathbf{C}$, and $\mathbf{G}$ are matrices of inertia, stiffness, stiffness due to transient motion, damping (that may include proportional damping), and gyroscopic (rotational speed dependent) effect. In addition, $\mathbf{F}_u$ and $\mathbf{F}_s$ are the vectors of external forces due to both the unbalance and to the suspension by pseudoelastic SMA wires, respectively. The FEM model considers four DOFs per node, namely, two displacements (along the directions x and z) and two rotations (around the axes x and z), respectively. For the simulation, the excitation force is due to unbalance and F_s is given by equation (12). The rotor-bearing system shown in Figure 4 was discretized into 16 nodes, as depicted in Figure 5. In this model, the suspension is located as close as possible to the bearing #2 (at node #16). The coupling is located at node #1, the bearing #1 is at the node #5, and the disk is placed at the node #12. The properties of bearings and coupling were obtained experimentally as shown by Alves (2015). These properties together with the rotor properties are presented in Table 1. For this rotor-bearing system, the mode shapes for the first and second modes are shown in Figure 6(a) and (b), respectively. It is important to mention that the first mode shape, as clearly shown, enhances the effectiveness of the suspension, just as defined its architecture. However, due to the discrepancy between the stiffnesses along both directions as discussed earlier, the gyroscopic effect takes place exactly in the second mode, precisely when the rotor-bearing system exhibits an extremely flat orbit along the vertical direction, such that the dynamics of the system has no action onto the suspension.

SMA constitutive model

The behavior of SMA for the 1D case is described by the constitutive models proposed by Brinson (1993), Brinson and Huang (1996), and Bekker and Brinson (1998). In this article, the focus is on the pseudoelastic

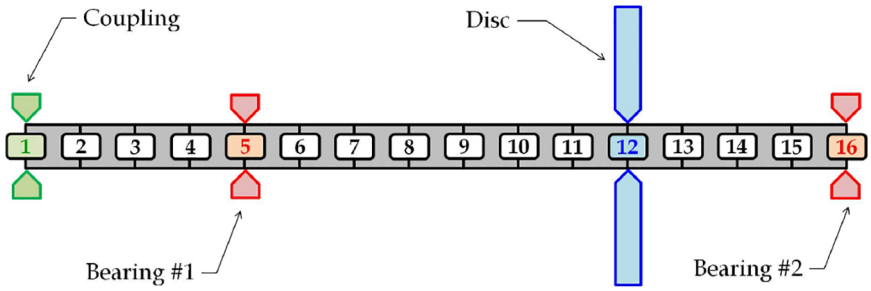

Figure 5. Schematic of shaft discretization.

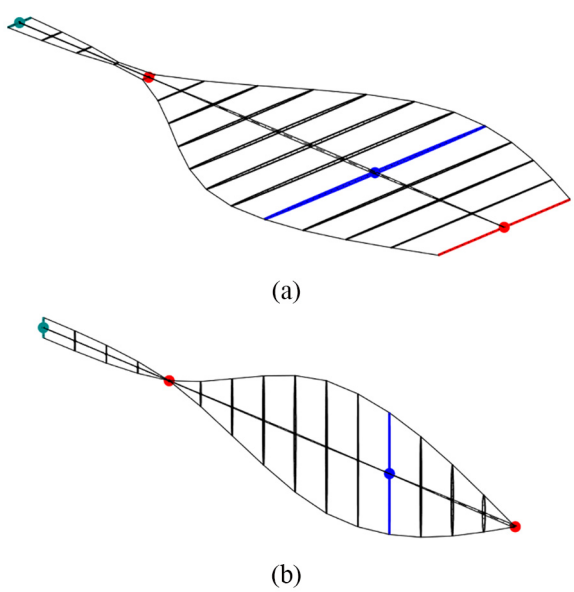

Figure 6. Mode shapes of the rotor-bearing system: (a) first mode and (b) second mode (green node → coupling; red nodes → bearings; and blue node → disk).

behavior of the material. Thus, we can neglect the twinned martensite since the lowest operational temperature (room temperature) is higher than the martensitic start temperature M_s for the material used in the SPW, as can be seen in Table 3. So, by considering the characteristic temperatures of SMA and the operational temperature range, the constitutive equation that governs its behavior is given by

$$\sigma = E(\epsilon - \epsilon_L \xi) \tag{3}$$

where σ is the axial stress, ϵ is the actual strain, ξ is de martensite volume fraction, and ϵ_L is the residual strain dependent upon each alloy. According to the original Brinson's model, both the twinned and detwinned martensite can coexist. However, only the detwinned martensite will be considered in this contribution. Furthermore, $E = E_A + \xi(E_M - E_A)$, where E_M and E_A are, respectively, Young's moduli for martensitic and austenitic crystallographic structures, and ε_L is the

Table 3. Thermomechanical properties for the PE SMA wire.

ϵ_L	Residual strain (%)	4.08
E_A	Young's modulus of austenite (GPa)	44.5
E_M	Young's modulus of martensite (GPa)	25.8
C_A	Stress influence coefficient of austenite (MPa/°C)	7.70
C_M	Stress influence coefficient of martensite (MPa/°C)	11.84
A_s	Austenitic start temperature (°C)	0.8
A_f	Austenitic finish temperature (°C)	17.0
M_s	Martensitic start temperature (°C)	11.8
M_f	Martensitic finish temperature (°C)	−6.5

residual strain due to phase transformation. It is important to mention that in the context of this contribution, some terms are not considered, such as thermoelastic expansion and any change in the material due to mechanical deformation (Enemark et al., 2014).

During the forward transformation, the evolution of the martensite volume fraction ξ is governed by

$$x_f = \frac{\sigma - \sigma_{m_s}}{\sigma_{m_f} - \sigma_{m_s}} \tag{4}$$

$$f_f = f(x_f) \tag{5}$$

$$\xi = \xi_0 + (1 - \xi_0) f_f \tag{6}$$

For the reverse transformation, one has

$$x_r = \frac{\sigma - \sigma_{a_s}}{\sigma_{a_s} - \sigma_{a_f}} \tag{7}$$

$$f_r = f(x_r) \tag{8}$$

$$\xi = \xi_0 f_r \tag{9}$$

where f_f and f_r are the so-called hardening functions. The mandatory requirement for this function is that the horizontal tangents at the boundaries ensure smooth transition between linearly elastic regions and transformation regions. Thus, the proposal is to use a cubic Bézier curve to control the parameters instead the one based on a cosine function, as originally considered in Brinson's model. The cubic Bézier curve, as shown in Figure 7, ensures genuine smoothness (infinitely differentiability) as shown previously by Alves et al. (2015). For more details regarding the mathematical

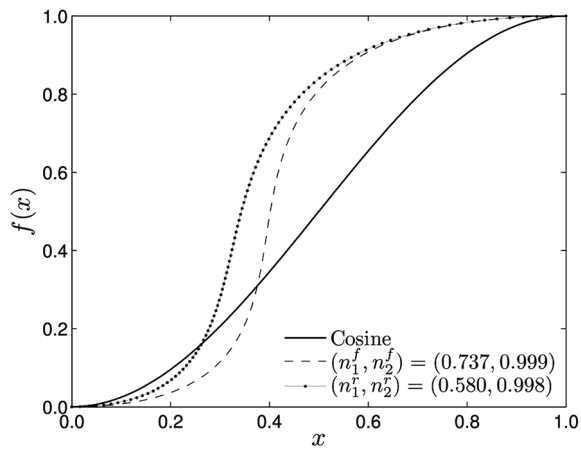

Figure 7. Hardening functions in the forward and reverse transformations.

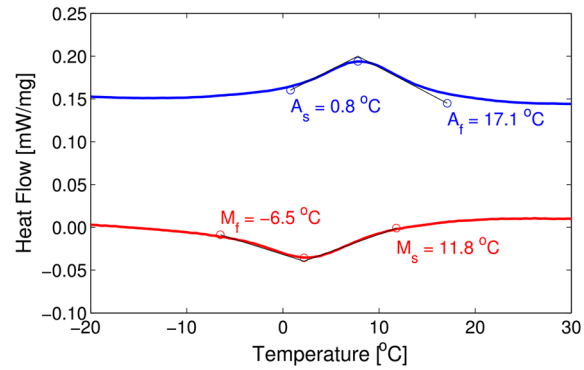

Figure 8. Differential scanner calorimetry test of the SMA wire.

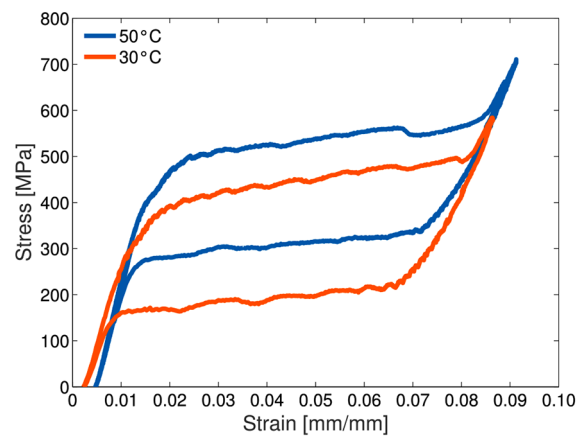

Figure 9. Tensile test of the SMA wire.

development, refer to Brinson and Huang (1996), Bekker and Brinson (1998), and Enemark and Santos (2016a).

The pseudoelastic SMA wires used in this contribution were purchased from website *Amazon*® accessing directly http://www.amazon.com/dp/B001385FYY/, and all their thermomechanical properties can be found in Table 3.

Thermomechanical characterization

Thermomechanical analysis of SMAs needs to establish a proper characterization that can identify the main aspects of the SMA. Basically, different experimental tests are developed to perform the characterization. Phase transformation temperatures are usually measured from differential scanning calorimetry (DSC) tests. Mechanical properties are evaluated from mechanical tests, usually performed with a universal testing machine.

Temperature plays an essential role in the thermoelastic martensite phase transformation and, therefore, physical properties, such as the electrical resistivity and elastic modulus, change with temperature. The determination of thermal properties is fundamental to the design of actuators based on SMAs, targeting advanced applications.

DSC analysis. The *Netzsch*® *DSC 200 F3* is the calorimeter model used to characterize the Ni-Ti wires of the test rig.

DSC test analyzes phase temperature of SMA sample by monitoring temperature and heating. The SMA sample is placed in a small crucible and measurements are compared with a reference sample, that can be a stable metal without phase transformation in the temperature range examined. The calorimeter makes measurements of temperature and energy occurring during the process, rate of 10°C/min is used for thermal characterization.

A typical measurement of the DSC test is presented in Figure 8 that shows phase transformation temperatures: M_s, M_f, A_s, and A_f. These temperatures represent the start and finish of martensitic formation and the start and finish of the formation of austenite. These measurements are done considering the tangent method.

Isothermal stress–strain tests. Mechanical properties are usually evaluated from universal testing machines. Cyclic tensile tests are performed using an INSTRON® Model 5902 with an environmental chamber. Figure 9 shows the stress–strain curve at temperatures around 30°C and 50 °C. A typical pseudoelastic curve is achieved where it is possible to identify elastic moduli of austenite and martensite, and a hysteresis loop associated with phase transformation. The elastic coefficients can be obtained by the slope of the linear elastic response. At the same time the C_A and C_M values can be obtained by tracing tangents at the stress versus strain curves.

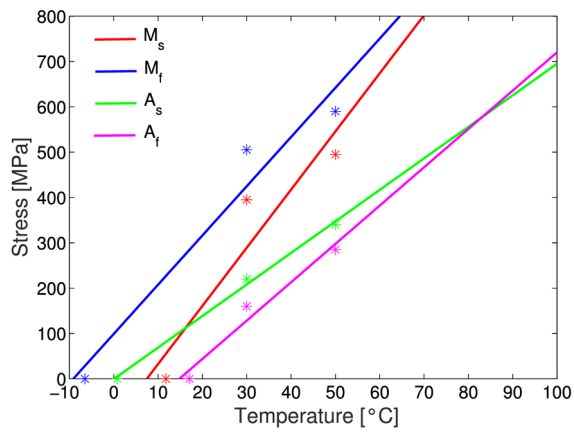

Figure 10. C_A and C_M from stress–strain tests for different temperatures.

According to Brinson (1993), the constants C_M and C_A are material properties that describe the relationship of temperature and the critical stress to induce transformation, σ_{crit}. The objective of this test is to establish the coupling between phase transformation critical stress and temperature, represented by the slopes of the curves in Figure 10. Both C_M and C_A adopted in this contribution correspond to the average between the slopes of the M_s and M_F, and A_s and A_F curves, respectively.

Table 3 presents a summary of the thermomechanical characterization.

Suspension by pre-tensioned wires model

Both Figures 11(a) and (b) illustrate schematically how the suspension (SPW) is connected to the bearing #2. Besides, these two figures illustrate the geometry of the suspension. In addition, some basic parameters for the problem formulation, such as $a_0 = x_p$, $a_1 = x_p - x_b$, and $a_2 = x_p + x_b$ that define how much tensioned the wires are (where x_p and x_b are, respectively, the pre-tension and bearing displacements) are written. Moreover, the parameter $b_0 = L$ is half-length of the wire. If the bearing #2 is still or is passing through the equilibrium position, only the pre-tension due to x_p is activated and consequently $\alpha_i = \tan^{-1}(a_i/b_0)$ can be defined. It is important to emphasize that this SMA elongation system actuates only at the bearing #2 along the x-axis. It should be noted that in the end the wires work as nonlinear springs. All these predefined parameters will be used later in the modeling of SPW.

Consequently, based on the aforementioned figures, the elongation of the wire can be expressed by $\Delta L = \epsilon_0 L$, where ϵ_0 is the engineering strain due to the pre-tension applied to the wires. Besides, using Pythagorean theorem, the parameters c_1 and c_2 are calculated in order to define the suspension geometry. Regarding the forces exerted by the suspension, due to the symmetry (upper and lower parts), it is necessary to

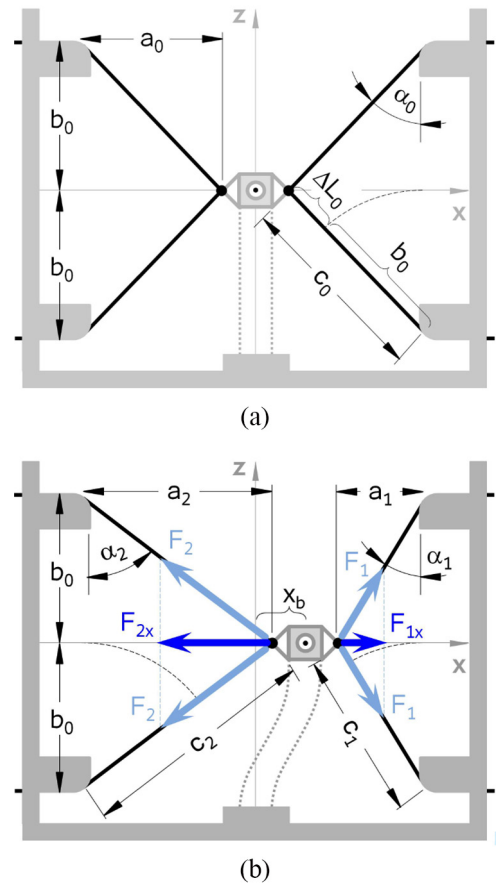

Figure 11. Schematic of the suspension system (SPW): (a) rotor at rest and (b) rotor in operation (dotted lines → flexible frame).

duplicate and project $F_1 = \sigma_1 A$ and $F_2 = \sigma_2 A$ on the x-axis. Therefore, based on geometrical relations found in Figure 11(b), the force F_{1_x} that pulls the bearing #2 to the right is given by

$$F_{1_x} = 2F_1 \sin\alpha_1 = 2F_1\left(\frac{a_1}{c_1}\right) = \frac{2\sigma_1 A[c_0 \sin\alpha_0 - x_b]}{\sqrt{x_b^2 - 2x_b c_0 \sin\alpha_0 + c_0^2}} \tag{10}$$

whereas the antagonistic force F_{2_x} is given by

$$F_{2_x} = 2F_2 \sin\alpha_2 = 2F_2\left(\frac{a_2}{c_2}\right) = \frac{2\sigma_2 A[c_0 \sin\alpha_0 + x_b]}{\sqrt{x_b^2 + 2x_b c_0 \sin\alpha_0 + c_0^2}} \tag{11}$$

where $c_0 = L(1 + \epsilon_0)$ is the length of wire due to pre-tension when the suspension is still, as previously described in Figure 11. Thus, according to the reference frame, the total force F_s applied by the SPW to the rotor through the bearing #2 can be written as

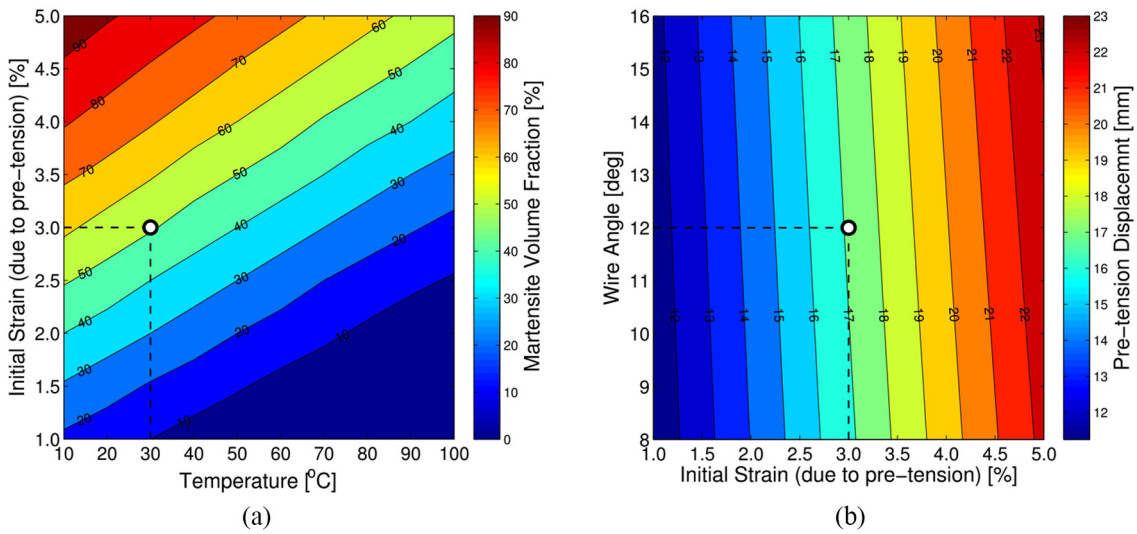

Figure 12. (a) Martensite volume fraction with respect to the initial strain (due to pre-tension) and to the temperature $\xi(\epsilon_0, T)$ and (b) pre-tension displacement with respect to the initial strain and the wire angle $x_p(\epsilon_0, \alpha_0)$.

$$F_s = F_{1_x} - F_{2_x} \tag{12}$$

As can be noticed, the forces F_{1_x}, F_{2_x}, and consequently F_s are dependent on the stress σ, which in turn is calculated and updated iteratively using the model described above in the section entitled "SMA constitutive model." It is worth remembering that F_s is an external force within the model described by equation (2). In other words, the compatibility between the model and the physics associated with the problem was preserved.

Calculating the pre-tension in the SPW. Here, using the formulation for the current SMA constitutive model together with the geometry of the SPW, two graphs are generated. The first relates the martensite volume fraction ξ with an initial strain ϵ_0 (due to pre-tension) and the temperature T, as shown in Figure 12(a). The other graph, as can be seen in Figure 12(b), relates the pre-tension displacement x_p with the initial strain ϵ_0 and the wire angle α_0 (as a consequence of x_p). As previously established, the goal is to provide only a tension region in the mechanical loading history. In order to guarantee this condition, a value for the pre-tension displacement x_p has been chosen such that $\xi_0 = 50\%$. As depicted in the figures mentioned above, the values for the parameters of interest are $x_p = 17$ mm (that yields an wire angle $\alpha_0 = 12°$) and $\epsilon_0 = 3\%$. In addition, the hysteresis effect is only significant at high pre-tension levels. Furthermore, it is worth mentioning that all these parameters are essential to initialize the computational code responsible to simulate the dynamic behavior of the rotor system suspended by SMA wires.

Results and discussion

The performance of the suspension (SPW) was tested for four operating conditions, namely, rotor at rest and transient rotation (*run-up*) for three different temperatures, besides steady-state rotation at first critical speed for several temperatures, and steady-state rotation at first critical speed with varying temperature. For the first test, the excitation comes from an impact, and for the other cases, the excitation is provided by the unbalance.

Impulse response with the rotor at rest for several temperatures

This test was performed with the rotor at rest for several temperatures, namely: $T = 30\,°C$, $T = 45\,°C$, and $T = 60\,°C$. In this sense, using an impact hammer, three frequency response functions were generated for the horizontal and vertical directions, as depicted in Figure 13(a) and (b), respectively, although the focus relies on the horizontal direction due to the suspension effectiveness in this condition. For this test, both that the excitation and the measurement sensor are located at the disk.

For this analysis, it is important to consider two points, namely: the phase transformation of SMA is dependent on the thermomechanical loading, and the suspension is only effective along to the horizontal direction. For the first mode, as shown in Figure 13(a), from the temperature $T = 30\,°C$ to $T = 45\,°C$, the thermal loading was enough to induce phase transformation to increase only the stiffness (denoted by the slight

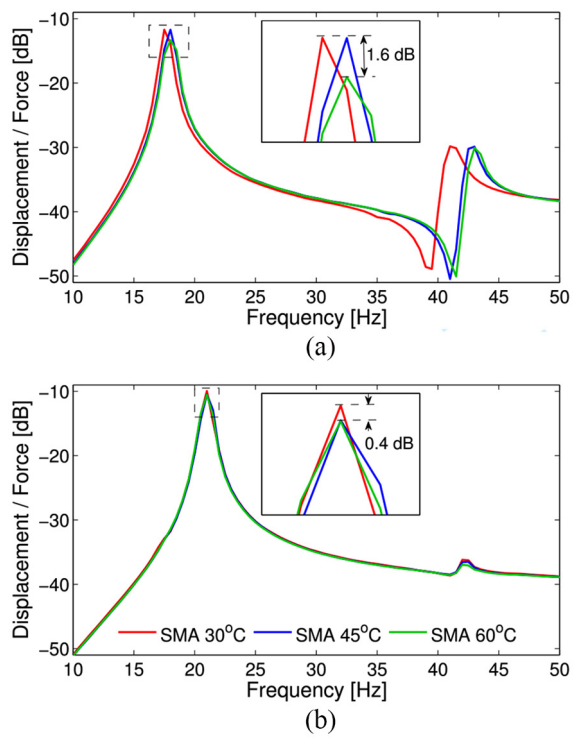

Figure 13. Experimental FRFs (estimated): (a) horizontal direction and (b) vertical direction.

Table 4. Summary for impulse response results—natural frequencies.

Temperature (°C)	Natural frequency (Hz)	Reduction (dB)
First mode (horizontal direction)		
30	17.5	–
45	18.0	0.0
60	18.0	1.6
Second mode (vertical direction)		
30	21.0	–
45	21.0	0.4
60	21.0	0.4

natural frequency shifting), whereas the mechanical loading (due to the impulsive excitation) was insufficient to induce an amount of hysteresis loops enough to increase the damping (denoted by no reduction in the peak). The other part, from $T = 45\,°C$ to $T = 60\,°C$, the thermomechanical loading provided a condition where the phase transformation resulted only in damping increase, as denoted by the reduction of 1.6 dB (or approximately 17%) in the peak. However, based on the estimation for the vertical direction depicted in Figure 13(b), there is no significant reduction since the peak associated with the second mode (around 21 Hz) was reduced only 0.4 dB (or approximately 4%). In the end, the explanation for these results is dependent on the weighting of each part of the thermomechanical loading that promotes the phase transformations as well as hysteresis cycles. In this article, the dissipated energy was not quantified, since only a qualitative analysis was performed. The results for both tests are summarized in Table 4.

Table 5. Comparison between experimental and simulated results—steady-state response at first critical speed for several temperatures.

Temperature (°C)	Experimental (mm)	Simulated (mm)	Deviation (%)
Bearing #2 (pk-pk)			
30	1.97	1.19	40
45	1.49	1.03	31
60	1.24	0.92	26
Disk			
30	0.81	1.08	−34
45	0.67	0.95	−42
60	0.48	0.90	−87

Based on the constitutive model evaluated in this contribution, the dynamic behavior obtained was expected from theory, once that, the higher the temperature, the lower the martensite volume fraction. In other words, the alloy (pseudoelastic wire) becomes stiffer since Young's modulus for the austenitic phase is 58% higher than the martensitic phase (see Table 3). However, the transient character of the impulse response leads to a transient phase transformation. Briefly, the mechanical loading vanishes quite rapidly over time, and for this reason, the hysteresis loop is not capable of dissipating an important amount of energy from the structure.

Steady-state response at first critical speed for several temperatures

This section presents both simulated and experimental steady-state responses for several temperatures, as depicted in Figures 14 and 15, respectively. The focus herein lies on showing only the responses along the horizontal direction. This decision is based on two reasons: first, only the first mode (that takes place along this direction) was evaluated in this contribution; second, the suspension (SPW) is only effective in this same direction. The alternative way to show these results is presented in Table 5, where the deviation rates are calculated considering experimental results as a reference.

In this case, from the point of view of vibration control, the suspension (SPW) accomplished its task. This statement is based on the results conveyed. In this operating condition, the vibration level is the highest, and

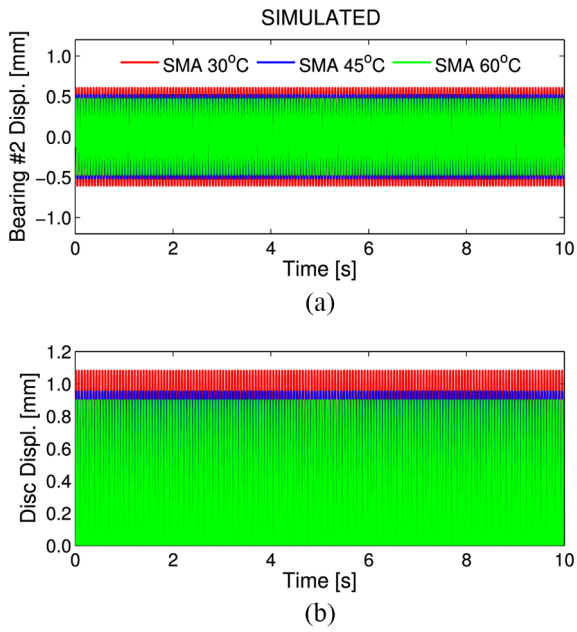

Figure 14. Simulated steady-state response at first critical speed and constant temperature in the SPW: (a) bearing #2 displacement (node #16) and (b) disk displacement (node #12).

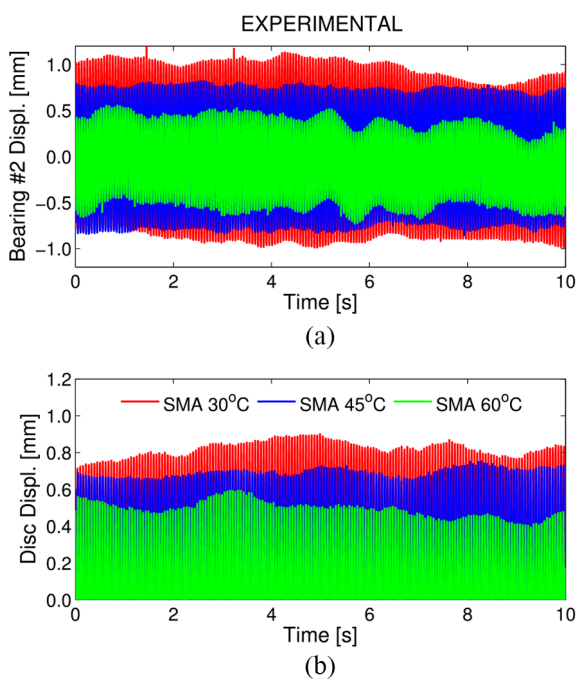

Figure 15. Experimental steady-state response at first critical speed and constant temperature in the SPW: (a) bearing #2 displacement and (b) disk displacement.

for this reason, the phase transformation takes place during all the time test. Figure 16 shows that hysteresis

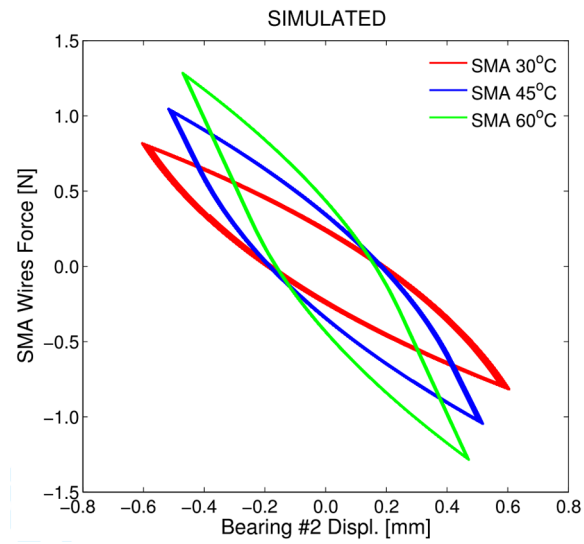

Figure 16. Simulated hysteresis loop at first critical speed and constant temperature in the SPW.

loop is more upward inclined for the higher temperature, such that the higher the temperature, the stiffer the suspension. It is worth mentioning that the shaft of the rotor-bearing system used in this work is very thin (only 6 mm) and therefore very flexible. In this case, by assuming a conventional material for the wire (such as the steel), as the bearing stiffness increases, the vibration amplitude of the disk increases as well (Muszynska, 2005). However, using pseudoelastic SMA wires, a stiffer suspension was capable of providing lower vibration amplitude for the disk, in such a way that it can be concluded that the main reason for the reported reductions is most likely due to energy dissipation.

Steady-state response at first critical speed with varying temperature

In this section, the results for numerical and experimental evaluations are presented. Here, the rotor operates at constant speed of rotation, and the suspension is submitted to varying temperature. It is important to say that the idea was to operate the rotor as close as possible to the first natural frequency. For this reason, in both cases, the speed of rotation was shifted only 2% from the respective natural frequencies. Thus, for the simulation and the experimental tests, the rotational speed was set to 984 and 1080 r/min, respectively. The choice of the rotation speed close to the critical speed is to provide large vibration amplitude, being enough to induce phase transformation in the SMA wires of the suspension. Regarding the heating process, Figures 17(a) and 18(a) show the temperature

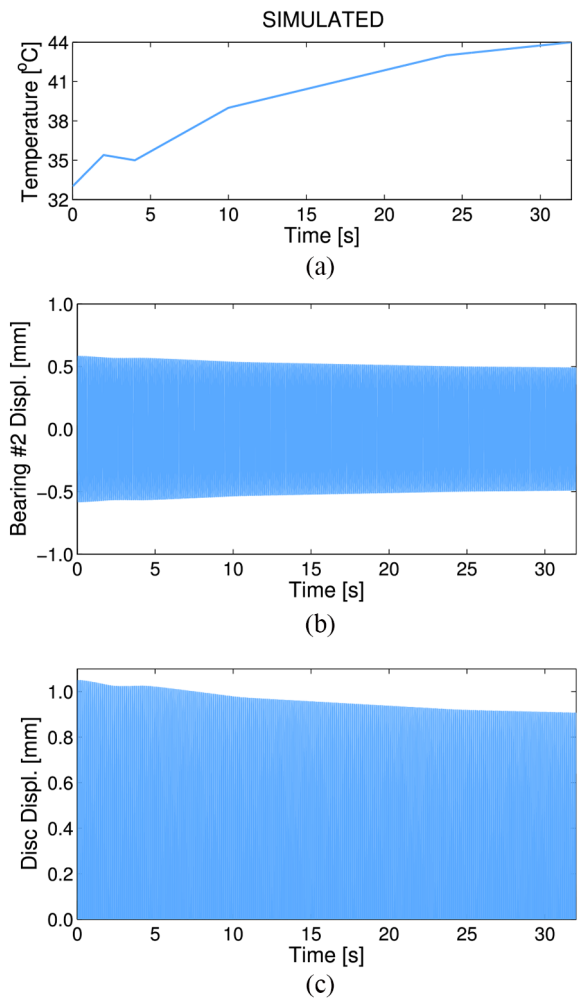

Figure 17. Simulated steady-state response at first critical speed and varying temperature in the SPW: (a) temperature time history, (b) bearing #2 displacement (node #16), and (c) disk displacement (node #12).

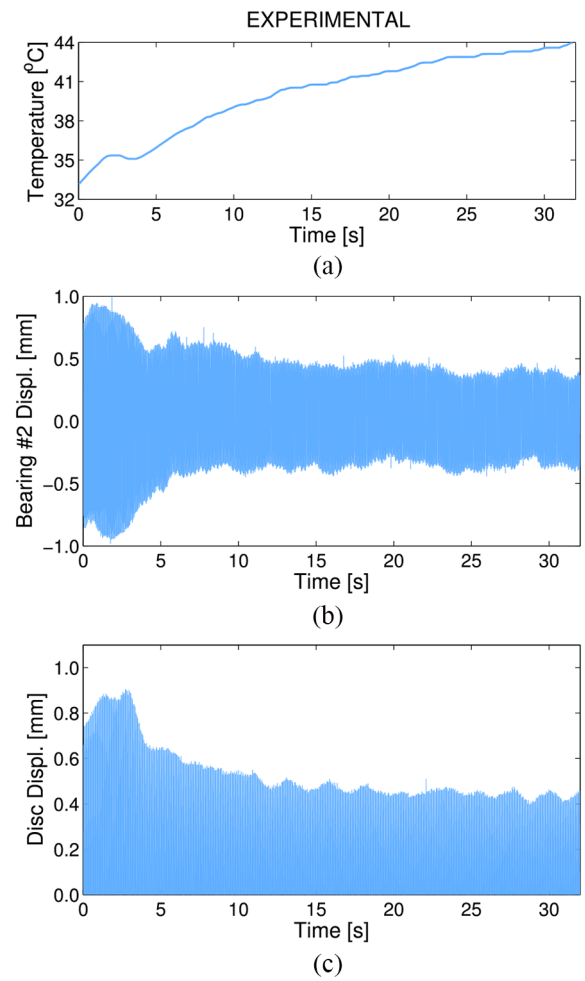

Figure 18. Experimental steady-state response at first critical speed and varying temperature in the SPW: (a) temperature time history, (b) bearing #2 displacement, and (c) disk displacement.

time history. In addition, note that the experimental curve was used to run the simulation test looking for more reliable results. As the suspension (SPW) was located at bearing #2, the presentation of the results begins with the corresponding displacements at this point, so that Figures 17(b) and 18(b) illustrate the simulated and the experimental cases, respectively. The simulated and experimental displacements of the disk are shown, respectively, in Figures 17(c) and 18(c). As done before, the hysteresis loops were simulated, specifically at $t = 2$ s and $t = 32$ s. Thus, the suspension stiffness increases over time, as revealed by Figure 19. This fact justifies the reduction of the vibration amplitude because the difference between the natural frequency (that increases over time) and the given operational frequency becomes larger. In other words, the rotor runs away from the resonant condition whenever the temperature increases. Therefore, all reduction rates regarding this evaluation can be observed in Table 6.

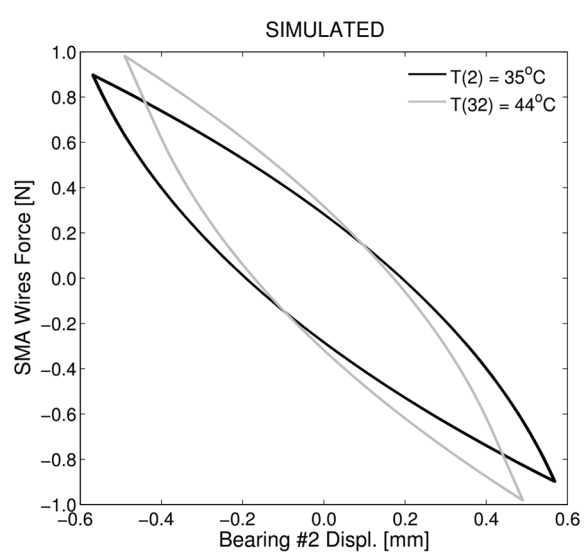

Figure 19. Simulated hysteresis loop at first critical speed and varying temperature in the SPW.

Table 6. Reduction rates for varying temperature evaluation.

	Experimental	Simulated
Bearing #2	64.6%	22.4%
Disk	51.9%	15.8%

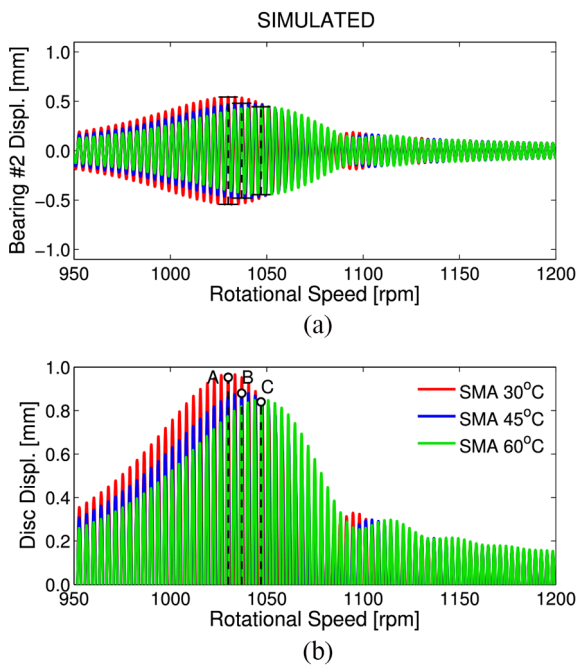

Figure 20. Simulated transient response: (a) bearing #2 displacement (node #16) and (b) disk displacement (node #12).

Transient response (run-up) for several temperatures

In this case, the unbalanced rotor was subjected to a constant acceleration of 60 r/min/s from stand still. The results for this scenario, both simulated and experimental, are presented, respectively, in Figures 20(a) and (b) and 21(a) and (b). As previously, the results are also shown in tabular form, as can be seen in Table 7. It is worth mentioning that only the range of interest (first mode) is focused on the studied application.

By observing the simulated and experimental responses, they do not correspond quantitatively. However, the difference found between the two cases are related to the assumptions that will be discussed later in this article. Another point is the fact that the critical speed of the rotor is temperature dependent, as commented and justified previously, where the higher the temperature, the larger the critical speed of the rotor, as can be seen in Table 8. Regarding the experimental case, two aspects were considered, as shown in Table 9. First, the focus relied on the response for each temperature; then, a potential way to cool down the wires in the suspension of the rotor was tested.

Table 7. Comparison between experimental and simulated results—transient response (*run-up*) speed for several temperatures.

Temperature (°C)	Experimental (mm)	Simulated (mm)	Deviation (%)
Bearing #2 (pk-pk)			
30	1.56	1.09	30
45	1.44	0.96	33
60	1.23	0.89	28
Disk			
30	0.77	0.95	−23
45	0.75	0.88	−17
60	0.63	0.84	−33

In the first experimental approach, considering the response for the temperature $T = 30\,°C$ as being the reference, the reduction rate, as presented in Table 9, is 2.6% from the point A to B, and 18.2% from the point B to C. For this last case, the result is interesting, especially because the power consumption to heat the suspension up to $T = 60\,°C$ in a few seconds is not high, since it is a *run-up* operation. However, for the second experimental approach (not performed in this work), a hypothetical scenario was considered, where the rotor (with the SMA wires of the suspension at $T = 45\,°C$ or $T = 60\,°C$) would pass through critical speed (represented by the reference response) during the rotor acceleration phase and immediately after this the suspension would be cooled rapidly, analogously to the principle used by Nie and Yan (2000), as can be observed in Figure 21(b). In this case, the estimated reduction rates are 24.9% from the point A to the point D and 55.8% from the point A to the point E. Therefore, for this case, the performance of the suspension is noticeably higher than the one revealed by the first approach. It is important to mention that, as for the first approach, the heating power consumption would not be an issue. Consequently, differently from what occurred in the section devoted to the response, here, the vibration of the rotor is higher and more lasting than the one that results from the impulse response, and for this reason, it is capable of inducing a high level of phase transformation in the SMA wires due to thermomechanical loading. Then, all these phenomena studied most likely represent a larger amount of dissipated energy or, in other words, more damping effect was added to the system despite of the stiffer suspension used, as justified in the section devoted to steady-state responses for the first critical speed.

Comments on the key assumptions

For all cases studied above, the performance of the suspension (SPW), as demonstrated by the experimental

Table 8. Comparison between experimental and simulated results—critical speeds (first mode) for transient response (*run-up*) speed for several temperatures.

Temperature (°C)	Critical speed (Hz)	
	Experimental	Simulated
30	17.6	17.2
45	17.8	17.3
60	18.2	17.5

results, was better than the results obtained from the simulation in terms of vibration reduction. This means that the performance of the model is deeply linked to the assumptions that were made to construct the model. These assumptions are now discussed in the following:

1. *The temperature along the wire is equal to the temperature of the environment*: in real world suspensions, the heating chamber is not hermetically sealed. Besides, its geometry is not able to provide a uniform air flow distribution and, consequently, an unequal thermal field results;
2. *Constant temperature in the wire cross-sectional area*: for this reason, the diameter of wire was chosen as 0.25 mm; however, this condition does not avoid a non uniform temperature distribution;
3. *Thermal expansion of SMA wire is neglected*: due to thermal expansion, the (stress-free) length of the SMA wires increases with temperature. This means the pre-tension length and pre-tension force decreases with temperature. This phenomenon is neglected in the model and could therefore be a strong assumption;
4. *Self-heating of SMA wire is neglected*: whenever a cyclic mechanical loading takes place self-heating is induced, which amplifies the effect of the environmental temperature;
5. *Thermomechanical properties of SMA wire are deterministic*: actually, no matter how good the characterization process is, the parameters always carry a certain level of uncertainty.

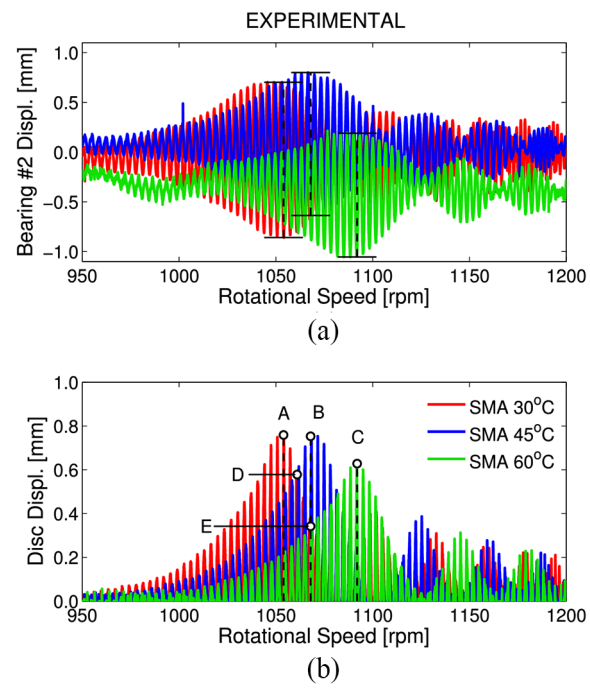

Figure 21. Experimental transient response: (a) bearing #2 displacement and (b) disk displacement.

Concluding remarks

Numerical simulations have been carried out for a rotor-bearing system suspended by pre-tensioned wires (SPW) in which pseudoelastic SMA wires are used to control the dynamic response of the system. In this sense, a modified Brinson's model was used to describe the SMA wire behavior when subjected to thermomechanical loading. It was shown that for all tests performed, the results reveal that the higher vibration and the higher temperature, the higher damping effect will be expected from the SMA suspension. This conclusion is supported by the amplitude reduction that was observed for the rotor-bearing system.

For the impulse response with the rotor at rest, the suspension was capable of reducing slightly the amplitude since the response due to impact vanishes rapidly in such a way that the duration of the phase transformation (migration from martensite to austenite and

Table 9. Simulated and experimental reduction rates for the disk displacements.

Simulated		Experimental			
Approach 1		Approach 1		Approach 2	
Temperature (°C)	Reduction (%)	Temperature (°C)	Reduction (%)	Temperature (°C)	Reduction (%)
30	–	30	–	30	–
45 (*AB*)	7.7	45 (*AB*)	2.6	45 (*AD*)	24.9
60 (*AC*)	11.8	60 (*AC*)	18.2	60 (*AE*)	55.8

vice versa) is extremely short. By analyzing the transient response, it was observed that the performance of the suspension was even better because in the *run-up* operation, and the amplitude vibration becomes larger as the rotor passes through the critical speed, thus potentializing the phase transformation and, consequently, the damping effect (energy dissipation). Besides, if the possibility of cooling the SMA suspension down after the rotor passes through the critical speed (baseline at $T = 30\,^{\circ}\mathrm{C}$) is assured, the performance is significantly enhanced. Specifically, in the test with the rotation speed close to the first critical speed and varying temperature, an interesting behavior was captured. In this case, the response showed that the vibration amplitude decreases as the temperature was increased. Consequently, this peculiar behavior suggests that a suspension built with pseudoelastic SMA wire could be applied to rotating machines as a safety device in cases where the vibration level is suddenly increased. Therefore, the machine shutdown is avoided until maintenance procedure is performed. Then, the previous technique suggests a *temporary self-healing* approach for the rotor-bearing system by implementing a control law.

It was demonstrated that the dynamic behavior of the system should be evaluated according to two important parameters, namely, the hysteresis and stiffness. An important result of the present investigation is that the numerical model was capable of providing a reasonable qualitative agreement with the experimental results. For this reason, a natural topic for further research is to investigate the assumptions that were made to construct the model of the rotor-bearing system suspended by SMA wires. Anyway, the overall results showed that the SMA is efficient to reduce the vibration level of the system and can be used as an alternative solution to passive vibration control of rotating systems. Another important point is that for relatively low temperatures (in comparison with room temperature), for low heating power consumption (heating for short periods), the vibration reduction was significant.

Finally, based on the results above, it is possible to say that SMA wires represent an interesting alternative for semi-active rotor vibration control. In addition, the use of SMA in this context complies with the requirement of low energy consumption, as expected for the so-called *eco-rotors*.

Declaration of conflicting interests

The author(s) declared no potential conflicts of interest with respect to the research, authorship, and/or publication of this article.

Funding

The author(s) disclosed receipt of the following financial support for the research, authorship, and/or publication of this article: The authors are thankful to Brazilian Research Agencies such as CNPq and CAPES (supported by process BEX 11550/12-0) and to the Technical University of Denmark (supported by FTP research project 12-127502). The authors are also thankful to CNPq and FAPEMIG Brazilian Research Agencies for their support through INCT-EIE.

ORCID iD

Valder Steffen Jr https://orcid.org/0000-0001-6124-2554

References

Alves MTS (2015) *Vibration control of rotating machinery using shape memory alloys*. PhD Thesis, Universidade Federal de Uberlândia, Uberlândia, Brazil (in Portuguese).

Alves MTS, Enemark S, Steffen V Jr, et al. (2015) Vibration control of a flexible rotor using shape memory alloy wires. In: *Proceedings of the XVII international symposium on dynamic problems of mechanics*, Natal, Brazil, 22–27 February.

Atepor L (2008) *Vibration analysis and intelligent control of flexible rotor systems using smart materials*. PhD Thesis, University of Glasgow, Glasgow.

Bekker A and Brinson LC (1998) Phase diagram based description of the hysteresis behavior of shape memory alloys. *Acta Materialia* 46: 3649–3665.

Borges JM, Silva AA, De Araújo CJ, et al. (2013) Rotor-bearing vibration control system based on fuzzy controller and smart actuators. *The International Journal of Multiphysics* 7(3): 197–205.

Brinson LC (1993) One-dimensional constitutive behavior of shape memory alloys: thermomechanical derivation with non-constant material functions and redefined martensite internal variable. *Journal of Intelligent Material Systems and Structures* 4: 229–242.

Brinson LC and Huang MS (1996) Simplifications and comparisons of shape memory alloy constitutive models. *Journal of Intelligent Material Systems and Structures* 7: 108–114.

Enemark S and Santos IF (2016a) Quasi-static characterisation of trained pseudoelastic shape memory alloy wire subjected to cyclic loading: transformation kinetics. *Journal of Intelligent Material Systems and Structures* 27(9): 1150–1164.

Enemark S and Santos IF (2016b) Rotor—bearing system integrated with shape memory alloy springs for ensuring adaptable dynamics and damping enhancement—theory and experiment. *Journal of Sound and Vibration* 369: 29–49.

Enemark S, Santos IF and Savi MA (2015) Shape memory alloys applied to improve rotor-bearing system dynamics—an experimental investigation. In: *Proceedings of the XVII international symposium on dynamic problems of mechanics*, Natal, Brazil, 22–27 February.

Enemark S, Savi MA and Santos IF (2014) Nonlinear dynamics of a pseudoelastic shape memory alloy system—

theory and experiment. *Smart Materials and Structures* 23: 085018.

Gupta K, Sawhney S, Jain SK, et al. (2003) Stiffness characteristics of fibre-reinforced composite shaft embedded with shape memory alloy wires. *Defence Science Journal* 53: 167–173.

He YY, Oi S, Chu FL, et al. (2007a) Vibration control of a rotor–bearing system using shape memory alloy: I. Theory. *Smart Materials and Structures* 16: 114.

He YY, Oi S, Chu FL, et al. (2007b) Vibration control of a rotor–bearing system using shape memory alloy: II. Experimental study. *Smart Materials and Structures* 16: 122.

Lalanne M and Ferraris G (1997) *Rotordynamics prediction in engineering*. 2nd ed. New York: John Wiley & Sons.

Lees AW, Jana S, Inman DJ, et al. (2007) The control of bearing stiffness using shape memory. In: *Proceedings of the IMAC-XXV: conference & exposition on structural dynamics*, Orlando, FL, 19–22 February.

Liu B, Yan L, Li Q, et al. (1994) Vibration control of a rotor system utilizing a bearing housing with controllable spring nonlinearity. In: *Proceedings of the ASME 1994 international gas turbine and aeroengine congress and exposition*, The Hague, 13–16 June, vol. 5, pp. V005T14 A007-1–V005T14A007-8. New York: ASME.

Ma Y, Zhang Q, Zhang D, et al. (2014) A novel smart rotor support with shape memory alloy metal rubber for high temperatures and variable amplitude vibrations. *Smart Materials and Structures* 23(12): 125016.

Muszynska A (2005) *Rotordynamics*. 1st ed. Boca Raton, FL: CRC Press.

Nagaya K, Takeda S, Tsukui Y, et al. (1987) Active control method for passing through critical speeds of rotating shafts by changing stiffnesses of the supports with use of memory metals. *Journal of Sound and Vibration* 113(2): 307–315.

Nie J and Yan X (2000) Intelligent bearing system for passing through critical speed of aeroengine rotor by changing stiffness using SMA wires. *Materials Science Forum* 327–328: 99–102.

Silva LC, Savi MA and Paiva A (2013) Nonlinear dynamics of a rotordynamic nonsmooth shape memory alloy system. *Journal of Sound and Vibration* 332: 608–621.

Yogaraju R, Ravikumar L, Saravanakumar G, et al. (2016) Feasibility and performance studies of a semi active journal bearing. *Procedia Technology* 25: 1154–1161.

Yuan H, Fauroux JC, Chapelle F, et al. (2017) A review of rotary actuators based on shape memory alloys. *Journal of Intelligent Material Systems and Structures* 28(14): 1863–1885.

Zhu ZW, Wang HL and Xu J (2009) Application on rotor vibration control of SMA model based on multivariate statistical analysis. In: *Proceedings of the world congress on computer science and information engineering*, Los Angeles, CA, 31 March–2 April.